

The M_w 5.8 Mineral, Virginia, Earthquake of August 2011 and Aftershock Sequence: Constraints on Earthquake Source Parameters and Fault Geometry

by Daniel E. McNamara, H. M. Benz, R. B. Herrmann, E. A. Bergman, Paul Earle,
Anne Meltzer, Mitch Withers, and Martin Chapman

Abstract The M_w 5.8 earthquake of 23 August 2011 (17:51:04 UTC) (moment, M_0 5.7×10^{17} N·m) occurred near Mineral, Virginia, within the central Virginia seismic zone and was felt by more people than any other earthquake in United States history. The U.S. Geological Survey (USGS) received 148,638 felt reports from 31 states and 4 Canadian provinces. The USGS PAGER system estimates as many as 120,000 people were exposed to shaking intensity levels of IV and greater, with approximately 10,000 exposed to shaking as high as intensity VIII. Both regional and teleseismic moment tensor solutions characterize the earthquake as a northeast-striking reverse fault that nucleated at a depth of approximately 7 ± 2 km. The distribution of reported macroseismic intensities is roughly ten times the area of a similarly sized earthquake in the western United States (Horton and Williams, 2012). Near-source and far-field damage reports, which extend as far away as Washington, D.C., (135 km away) and Baltimore, Maryland, (200 km away) are consistent with an earthquake of this size and depth in the eastern United States (EUS).

Within the first few days following the earthquake, several government and academic institutions installed 36 portable seismograph stations in the epicentral region, making this among the best-recorded aftershock sequences in the EUS. Based on modeling of these data, we provide a detailed description of the source parameters of the mainshock and analysis of the subsequent aftershock sequence for defining the fault geometry, area of rupture, and observations of the aftershock sequence magnitude–frequency and temporal distribution. The observed slope of the magnitude–frequency curve or b -value for the aftershock sequence is consistent with previous EUS studies ($b = 0.75$), suggesting that most of the accumulated strain was released by the mainshock. The aftershocks define a rupture that extends between approximately 2–8 km in depth and 8–10 km along the strike of the fault plane. Best-fit modeling of the geometry of the aftershock sequence defines a rupture plane that strikes N36°E and dips to the east-southeast at 49.5°. Moment tensor solutions of the mainshock and larger aftershocks are consistent with the distribution of aftershock locations, both indicating reverse slip along a northeast–southwest striking southeast-dipping fault plane.

Online Material: Tables of regional moment tensor source parameters and aftershock location.

Introduction

A passive margin is the one formed by rifting followed by seafloor spreading such that the resulting tectonic plate consists of both continental and oceanic lithosphere. The Appalachian passive margin of the eastern United States (EUS) extends for 3300 km from northeastern Canada to

the southeastern United States (Fig. 1) and is among the most widely studied and geologically understood of modern passive margins (Bradley, 2008). Despite this, the passive margin of the EUS is inconsistent with a fundamental principal of plate tectonics that assumes tectonic plates are rigid and

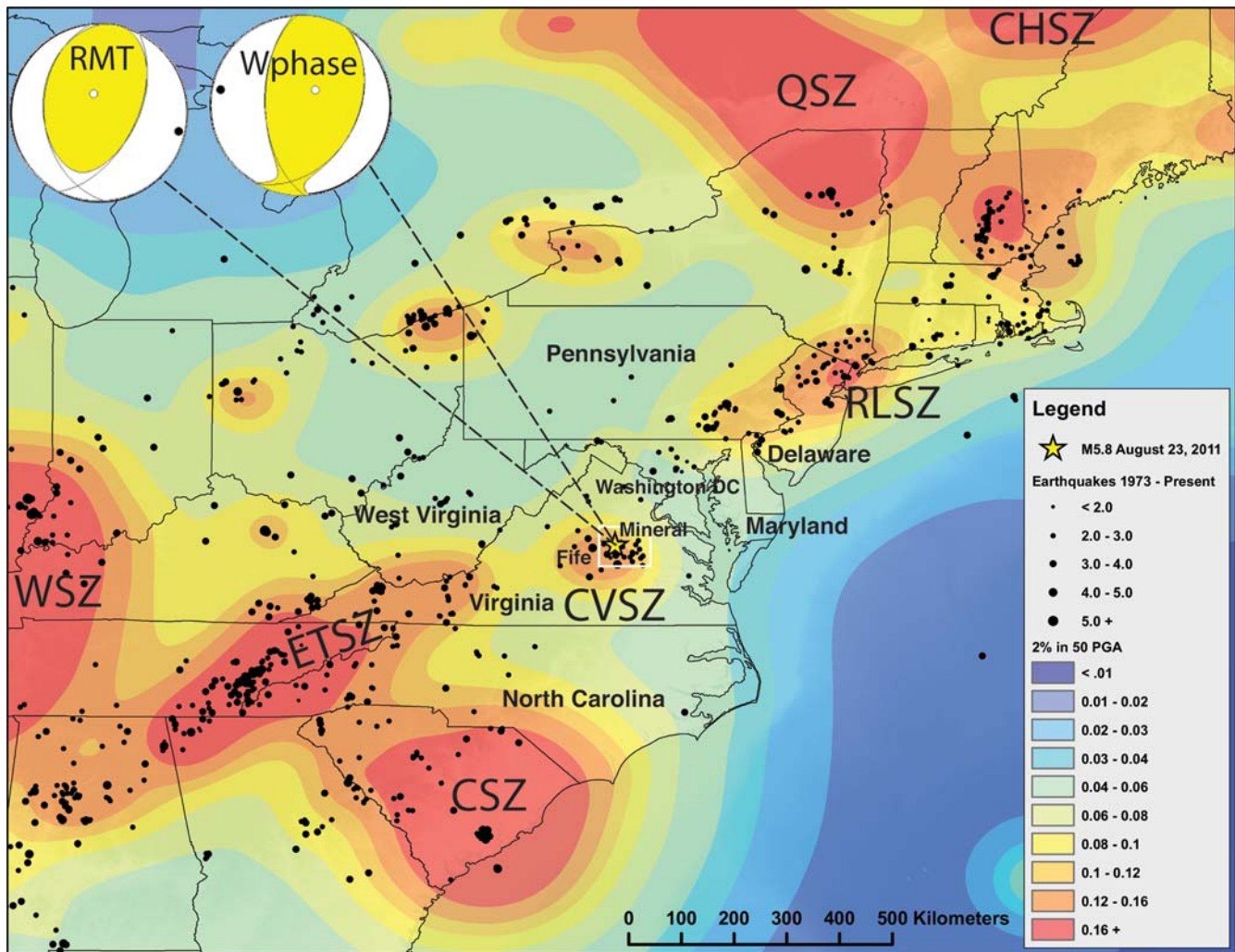


Figure 1. The probabilistic seismic hazard (Petersen *et al.*, 2008) and previous instrumentally recorded earthquakes in the region (black circles). Color contours represent the percentage of gravity that have a 2% chance of being exceeded in 50 years. The ANSS/CERI location of the M_w 5.8 Mineral, Virginia, earthquake on 23 August 2011 at 17:51 UTC is shown as a yellow star (37.936, 77.933). Also shown are mainshock reverse-faulting focal mechanisms determined from regional-waveform (RMT) and W -phase moment tensor modeling. Major seismic source zones shown in the region are the eastern Tennessee seismic zone (ETSZ), Wabash Valley seismic zone (WSZ), Charleston seismic zone (CSZ), Quebec seismic zone (QSZ), Charlevoix seismic zone (CHSZ), Reading–Lancaster seismic zone (RLSZ), and the central Virginia seismic zone (CVSZ). The white box outlines the region mapped in Figure 2.

deform at their edges (Wilson, 1965). In reality, the passive continental margin of the EUS can produce large and damaging earthquakes as highlighted by numerous historic events that contribute to relatively high-hazard regions in the U.S. Geological Survey (USGS) National Probabilistic Seismic Hazard Map (Fig. 1; Petersen *et al.*, 2008). Throughout the EUS, historical seismicity, geomorphic, and paleoseismic data indicate active but poorly understood tectonic processes within seismic source zones such as the New Madrid, Wabash Valley, the eastern Tennessee seismic zone (ETSZ), central Virginia seismic zone (CVSZ), and Reading–Lancaster seismic zone (RLSZ) (Wolin *et al.*, 2012). The M_w 5.8 earthquake on 23 August 2011 (17:51 UTC) near Mineral, Virginia, occurred within the northern portion of the well-known CVSZ (Fig. 1), a source region that has been mapped as an area of elevated seismic hazard since 1976 based on the

small-to-moderate size earthquakes documented since at least the eighteenth century (Algermissen and Perkins, 1976).

The earliest reported earthquake in the CVSZ occurred on 21 February 1774 and caused extensive damage in Petersburg, Virginia (Fig. 1). The largest historical earthquake in the CVSZ occurred in 1875 and shook bricks from chimneys, broke plaster and windows, and overturned furniture in the Richmond area, at which modified Mercalli intensity (MMI) levels of VI–VII were reported (Bollinger and Hopper, 1971). The felt area of the 1875 shock suggests it had a magnitude of about 4.8 (Campbell, 1898; Bollinger, 1969; Bollinger and Hopper, 1971). More recently, a pair of magnitude 4 earthquakes, separated by 12 s, occurred on 9 December 2003 and produced minor damage in Fife, Virginia, 60 km west of Richmond. In the month following the earthquakes, no aftershocks were felt nor recorded by a temporary

deployment of seismometers (Kim and Chapman, 2005). Seismicity in the region occurs along pre-existing zones of crustal weakness aligned with relic structures associated with past plate collisions and rifting episodes (Chapman, 2005, 2013). Instrumentally recorded seismicity in the CVSZ is generally shallow and distributed over a broad areal region with source depths averaging around 8 km. This seismicity is generally not clearly associated with mapped Paleozoic and Mesozoic geologic faults (Fig. 1) (Chapman, 2005).

The August 2011 M_w 5.8 Mineral, Virginia, earthquake (Fig. 1) had a reverse fault, compound rupture process, with three known subevents that occurred on a northeast-striking plane (Chapman, 2013). The earthquake distinguishes itself as one of the most widely felt earthquakes in United States history. The large felt area reported by the USGS “Did You Feel It?” (DYFI) system (Wald *et al.*, 2011) is roughly 10 times the area of a similarly sized earthquake in the western United States (Horton and Williams, 2012). The felt area extends north–south from central Georgia to southeast Canada and west to Detroit, Michigan, and Chicago, Illinois. Strong shaking from the earthquake caused significant damage to homes and permanently closed two schools in the epicentral area. In addition, North Anna nuclear power station shut down due to high recorded accelerations at the plant and remained closed for 2.5 months. A strong-motion accelerometer at the North Anna nuclear power plant recorded the closest known instrumental ground motions of the earthquake, in which the maximum horizontal acceleration reached 0.27g (Chapman, 2013). This is the first known case in which an operating nuclear power plant in the United States was closed in response to an earthquake (Earthquake Engineering Research Institute [EERI], 2011; Horton and Williams, 2012).

Structural damage to buildings was variable around the epicenter with brick and unreinforced masonry buildings performing poorly (EERI, 2011). The earthquake caused widespread light-to-moderate damage from central Virginia to southern Maryland, including the Washington Monument and the National Cathedral in Washington, D.C. Moderately heavy damage (MMI VIII) occurred in a rural area of Louisa County, southwest of Mineral, Virginia (Hough, 2012). Damage in Louisa County alone is estimated to be more than \$80 million. Repairs due to damage to the Washington Monument and the Washington National Cathedral are projected to cost \$40 million (Horton and Williams, 2012). Minor damage was reported in parts of Delaware, southeastern Pennsylvania, and southern New Jersey. The earthquake was very strongly felt (MMI VII) at Bumpass, Kent Store, Louisa, Mineral, Rhoadsville, and Summerduck in Virginia and felt strongly in much of central Virginia and southern Maryland.

The Earth science community lacks a comprehensive tectonic model to explain the distribution of EUS seismicity in space and time. It is generally assumed that passive margin seismicity occurs along zones of pre-existing weakness that are aligned with structures associated with ancient plate collisions and rifting, however, the driving forces remain unclear. Proposed mechanisms include plate wide forces

due to topographic processes such as ridge push and mantle flow beneath the continent as well as more localized stresses due to offshore sediment loading or deglaciation (Stein *et al.*, 1989; Wolin *et al.*, 2012).

The infrequent occurrence of significant earthquakes in the EUS limits the necessary observations needed to understand earthquake processes and to reduce uncertainty in seismic-hazard maps. For these reasons, characterizing the aftershock sequence of the 2011 Mineral, Virginia, earthquake offers a rare opportunity to improve our understanding of earthquake processes and earthquake hazard in this populous region of the United States. In this report we provide a comprehensive analysis of nearly one year of aftershocks recorded on both the permanent regional seismic network and temporary seismic stations deployed in the epicentral area of 2011 Mineral, Virginia, earthquake. Modeling from this study enables us to place constraints on the geometry of the active fault using detailed source parameters of the mainshock and large aftershocks. We also show the magnitude–frequency distribution of the aftershock sequence and interpret these results in order to improve our understanding of earthquake processes. In addition to this study, research is under way to better understand the geologic and geophysical setting of the M_w 5.8 central Virginia earthquake and the severity and distribution of seismic shaking, associated ground deformation and failures, geologic amplification characteristics of seismic recording sites (W. Stephenson, J. Odum, and D. E. McNamara, unpublished manuscript, 2013; D. E. McNamara, *et al.*, unpublished manuscript, 2014), and regional ground-motion attenuation (McNamara, Gee, *et al.*, 2014).

Temporary Aftershock Deployments

Within the first few days of the M_w 5.8 Mineral, Virginia, earthquake, multiple government and academic institutions deployed seismic instruments near the epicenter with the primary goal of recording aftershocks for postearthquake assessment of EUS seismic hazards. A total of 36 temporary seismograph stations were deployed and used in this analysis (Fig. 2, Table 1). Institutions involved in aftershock monitoring included Virginia Tech (XY; 7 stations), University of Memphis (ET; 4 stations), Lehigh University, Incorporated Research Institutions in Seismology (IRIS) (YC; 7 stations), and the USGS (GS, NQ, NP; 18 stations). The coordinated temporary deployment of seismic stations had three primary objectives: (1) to record and document the distribution of aftershocks to delineate the causative fault and constrain the dimensions of the rupture zone; (2) to improve estimates of earthquake source parameters (e.g., moment tensor solutions); and (3) to measure high-frequency (>0.5 Hz) ground-motion attenuation. In order to achieve these objectives, many of the aftershock recording systems included both broadband and strong-motion sensors.

All temporary stations were deployed within five days of the mainshock; eight were installed within 24 hours, just in time to record the largest aftershock (M_w 3.9) on 25 August

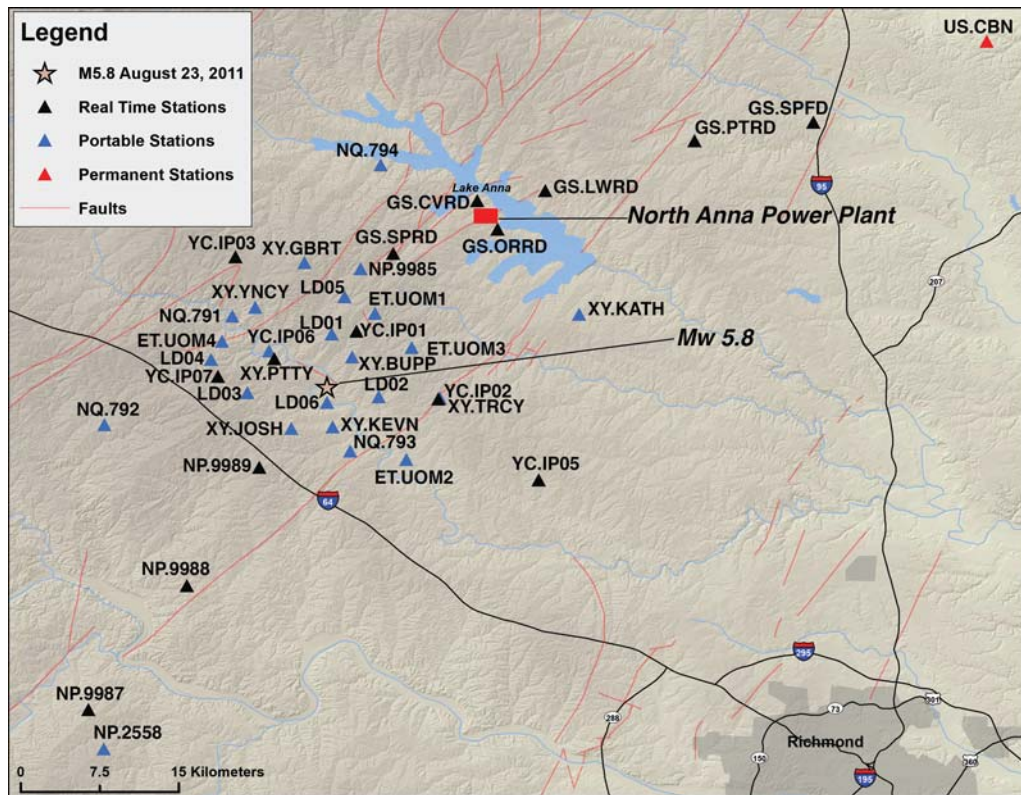


Figure 2. The distribution of seismic stations deployed in the epicentral region after the M_w 5.8 Mineral, Virginia, earthquake on 23 August 2011 at 17:51:04 UTC. The ANSS/CERI network location of the M_w 5.8 Mineral, Virginia, earthquake on 23 August 2011 at 17:51 UTC is shown as a star. Permanent seismic monitoring stations are shown as red triangles. Temporary non-real-time stations, deployed to record the aftershock sequence, are shown as blue triangles. Aftershock stations that contributed data directly to the ANSS/USGS for real-time earthquake monitoring are shown as black triangles. Red lines are taken from the USGS faults and folds database (Machette *et al.*, 2004). The approximate location of the North Anna nuclear power plant is shown as a red box.

2011 (© Table S1, available in the electronic supplement to this article). All stations recorded data continuously onsite, typically sampling the broadband channels at 100 samples/sec and strong-motion channels at 200 samples/sec. Twenty five of the portable stations were telemetered to the USGS National Earthquake Information Center (NEIC) allowing real-time monitoring of the aftershock sequence for nearly one year. All systems operated for the first few weeks of the aftershock sequence, during its most energetic phase. Smaller subsets of stations operated into the summer of 2012 (YC; Table 1). The final stations were removed in August 2012 (GS; Table 1). Figure 2 shows the distribution of both permanent and temporary aftershock seismograph stations in the vicinity of the mainshock.

Both the broad areal distribution of permanent stations, combined with the portable stations temporarily deployed within the epicentral region, enabled detection and location of a complete earthquake catalog down to approximately M_L 1.1. Table 1 provides a list of key stations and their attributes used in this modeling study. The high sample rate data and on-scale recording enabled us to determine source location, depth, and moment tensor solutions for significant aftershocks. In addition, these stations were used to evaluate

regional attenuation (McNamara, Gee, *et al.*, 2014) as well as local site conditions (D. E. McNamara, *et al.*, unpublished manuscript, 2014).

Another component of the postearthquake field investigations was the Aftershock Imaging with Dense Arrays (AIDA) study. Through AIDA, 117 EarthScope Flexible Array “Texans” were deployed between 27 August and 9 September 2011 in a series of densely spaced linear arrays (200–400 m station spacing over distances of 7–12 km), and 30 Texans were deployed as three-component stations in a 60 km linear array (Brown *et al.*, 2012). This was the first time that so many densely spaced instruments were deployed in the wake of a significant earthquake within the United States. Although the data from these instruments could be integrated with the other stations used to characterize the aftershock source parameters, we did not use them in this study because of their short duration of deployment relative to the length of the aftershock sequence, thus limiting their use in fully documenting aftershock source parameters. Their value primarily lies in being able to better understand detailed variations of high-frequency ground motion and attenuation as a function of distance from a few well-located aftershocks.

Table 1
Stations Used in This Study

Net.Station	Latitude (°)	Latitude (°)	Elevation (m)	Sensor Type
ET.UOM1	37.97224	-77.89543	140	Strong motion
ET.UOM2	37.84763	-77.86858	140	Strong motion
ET.UOM3	37.94324	-77.86408	140	Strong motion
XY.BUPP	37.93508	-77.91499	127	Short period
XY.JOSH	37.87000	-77.97000	128	Strong motion
XY.KEVN	37.88000	-77.93000	102	Strong motion
XY.KATH	37.97000	-77.92000	94	Short period
XY.PTTY	37.94000	-77.99000	98	Short period
XY.YNCY	37.97751	-77.99771	120	Short period
XY.TRCY	37.90018	-77.84018	114	Short period
NQ.791	37.97006	-78.01733	109	Strong motion
NQ.792	37.87722	-78.12663	129	Strong motion
NQ.793	37.85474	-77.91676	117	Strong motion
NQ.794	38.09906	-77.89056	91	Strong motion
NQ.RSTON	38.94810	-77.36750	122	Strong motion
NQ.WNC	38.93050	-77.0716	117	Strong motion
GS.CVRD	38.0686	-77.8081	100.1	Broadband, Strong motion
GS.LWRD	38.0771	-77.7501	120.0	Broadband, Strong motion
GS.ORRD	38.0442	-77.7908	104.0	Broadband, Strong motion
GS.PTRD	38.1196	-77.6227	75.0	Broadband, Strong motion
GS.SPFD	38.1353	-77.5211	79.0	Broadband, Strong motion
GS.SPRD	38.0234	-77.8800	110.0	Broadband, Strong motion
NP.2559	38.0037	-78.4536	100.0	Strong motion
NP.9985	38.0105	-77.9077	100.0	Strong motion
NP.9986	37.4861	-78.2563	109.0	Strong motion
NP.9987	37.6341	-78.1401	82.0	Strong motion
NP.9988	37.7399	-78.0562	92.0	Strong motion
NP.9989	37.8410	-77.9944	102.0	Strong motion
YC.IP01	37.9572	-77.9112	109.0	Broadband
YC.IP02	37.8992	-77.8415	115.0	Broadband
YC.IP03	38.0205	-78.0147	152.0	Broadband
YC.IP04	38.0922	-78.0942	166.0	Broadband
YC.IP05	37.8303	-77.7557	108.0	Broadband
YC.IP06	37.9334	-77.9815	114.0	Broadband
YC.IP07	37.9185	-78.0296	138.0	Broadband
CO.CSB	32.9870	-80.0715	6.0	Broadband
CO.JSC	34.2818	-81.2597	102.5	Broadband
CO.RGR	32.9075	-80.1940	10.0	Broadband
ET.CPCT	35.4500	-84.5220	275.0	Broadband
ET.SWET	35.2160	-85.9320	581.0	Broadband
IM.TKL	35.6580	-83.7740	351.0	Broadband
IU.HRV	42.5064	-71.5583	200.0	Broadband
IU.SSPA	40.6358	-77.8876	270.0	Broadband
IU.WCI	38.2289	-86.2939	78.0	Broadband
IU.WVT	36.1297	-87.8300	170.0	Broadband
LD.ACCN	43.3843	-73.6678	340.0	Broadband
LD.ALLY	41.6492	-80.1448	390.0	Broadband
LD.BRNJ	40.6828	-74.5660	50.0	Broadband
LD.CPNY	40.7911	-73.9602	27.0	Broadband
LD.FRNY	44.8350	-73.5883	242.4	Broadband
LD.KSCT	41.7261	-73.4842	114.0	Broadband
LD.KSPA	41.5570	-75.7682	298.0	Broadband
LD.LUPA	40.5987	-75.3718	255.0	Broadband
LD.MDV	43.9992	-73.1812	134.0	Broadband
LD.MIV	44.0747	-73.5340	317.0	Broadband

(continued)

Table 1 (Continued)

Net.Station	Latitude (°)	Latitude (°)	Elevation (m)	Sensor Type
LD.MMNY	42.7319	-77.9066	241.0	Broadband
LD.MSNY	44.9983	-74.8620	55.0	Broadband
LD.MVL	39.9992	-76.3506	91.0	Broadband
LD.NCB	43.9734	-74.2228	575.0	Broadband
LD.ODNJ	41.0829	-74.6056	187.0	Broadband
LD.PAL	41.0056	-73.9079	66.0	Broadband
LD.SDMD	39.4102	-76.8403	212.0	Broadband
LD.WVNY	42.4062	-78.6042	490.0	Broadband
NE.BCX	42.3350	-71.1705	60.0	Broadband
NE.BRYW	41.9170	-71.5378	107.0	Broadband
NE.DUNH	43.1370	-70.9348	53.0	Broadband
NE.FFD	43.4700	-71.6538	131.0	Broadband
NE.HNH	43.7052	-72.2865	180.0	Broadband
NE.QUA2	42.2790	-72.3522	168.0	Broadband
NE.TRY	42.7313	-73.6664	89.0	Broadband
NE.VT1	44.3206	-72.7513	149.0	Broadband
NE.WES	42.3848	-71.3218	60.0	Broadband
NE.WSPT	41.1710	-73.3275	70.0	Broadband
NE.YLE	41.3165	-72.9208	10.0	Broadband
NM.BLO	39.1719	-86.5222	246.0	Broadband
NM.OLIL	38.7338	-88.0991	150.0	Broadband
NM.PLAL	34.9824	-88.0755	165.0	Broadband
NM.SIUC	37.7085	-89.2401	118.0	Broadband
NM.USIN	37.9650	-87.6660	170.7	Broadband
NM.UTMT	36.3497	-88.8636	110.0	Broadband
PE.NCAT	36.0790	-79.7712	243.0	Broadband
PE.PAGS	40.2278	-76.7221	120.0	Broadband
PE.PSUB	39.9274	-75.4514	110.0	Broadband
TA.KMSC	35.1420	-81.3333	240.0	Broadband
TA.M54A	41.5079	-79.6647	488.0	Broadband
TA.N54A	40.9617	-79.9892	408.0	Broadband
TA.N59A	40.9168	-75.7703	508.0	Broadband
TA.O56A	40.2683	-78.5663	684.0	Broadband
TA.SFIN	40.3790	-87.0967	165.0	Broadband
TA.TIGA	31.4389	-83.5898	109.0	Broadband
US.AAM	42.3012	-83.6567	172.0	Broadband
US.ACSO	40.2319	-82.9820	288.0	Broadband
US.BINY	42.1993	-75.9861	498.0	Broadband
US.BLA	37.2113	-80.4205	634.0	Broadband
US.CBN	38.2046	-77.3732	70.0	Broadband
US.CNNC	35.2393	-77.8901	29.0	Broadband
US.ERPA	42.1175	-79.9891	306.3	Broadband
US.GLMI	44.8245	-84.6175	387.0	Broadband
US.GOGA	33.4112	-83.4666	-16.1	Broadband
US.LBNH	44.2401	-71.9259	367.0	Broadband
US.LONY	44.6197	-74.5829	440.0	Broadband
US.LRAL	33.0348	-86.9978	130.0	Broadband
US.MCWV	39.6581	-79.8456	280.0	Broadband
US.NHSC	33.1067	-80.1778	11.0	Broadband
US.TZTN	36.5439	-83.5490	394.0	Broadband

To improve the long-term monitoring of the area, the USGS installed permanent strong-motion seismograph stations at the U.S. Capitol, Washington Monument, National Cathedral, and in the Mineral, Virginia, epicentral area. In addition, the EarthScope Transportable Array installed earlier than scheduled, August 2012, a broadband station within the CVSZ. In early 2013, EarthScope installed a grid of broadband stations (approximately 70 km station spacing) in

Virginia as part of the USArray Transportable Array (TA). By fall 2013 the TA will be deployed throughout the EUS and will operate continuously for about 18 months.

Processing and Modeling Aftershock Data

One main objective of the aftershock deployment was to better image the causative fault(s) using improved earthquake locations based on an ensemble network of permanent regional seismograph stations and the dense network of temporary stations (Table 1). Initial locations of the aftershocks associated with the M_w 5.8 Mineral, Virginia, earthquake were determined with a standard single-event approach using a stand-alone version of the main processing and analysis system (also known as Hydra) used by the USGS NEIC (Buland *et al.*, 2009). This system allowed us to identify and locate individual earthquakes, compute network-averaged regional magnitudes (e.g., M_L , m_{bLG} , M_d), and M_w from waveform modeling of earthquakes larger than about M_w 3.5. The output from the automatic processing and review is a catalog of well-located earthquakes using data from both the permanent regional network and the temporary deployment (Table 1). A three-step approach was used for initial processing of the waveform data. First, all publicly available waveform data were loaded into an instance of the USGS NEIC operational processing system in which earthquake P -wave and S -wave phases were automatically picked, associated into common events and source parameters determined (location, magnitude). Second, the automatic locations and magnitudes were manually reviewed to improve the seismic-phase arrival-time picks and to add new secondary phases as available. This primarily included first arriving S waves that the automatic process did not identify. Finally, the continuous waveform data were visually reviewed to find small events that the automatic process missed. In the initial standard single-event approach, the aftershocks were located using the AK135 1D global velocity model (Kennett *et al.*, 1995) that is routinely used by NEIC. The final output from this analysis is a catalog of well-located earthquake (Table 1). A total of 454 earthquakes greater than about M_w 1.0 were located between 23 August 2011 and 30 July 2012, with six events in the magnitude range M_w 3.0–3.9. We did not locate all observed earthquakes, but only those events for which there was a sufficient number of arrival-time observations and good azimuthal coverage to ensure a well-constrained hypocenter. Typically, smaller earthquakes were only recorded on a few stations, making it difficult to accurately determine location and depth.

Calibrated Earthquake Relocations: Hypocentroidal Decomposition

After initial single-event aftershock locations and magnitudes were determined, using the procedures described above, they were reanalyzed to further refine source locations using a multiple-event approach based on the hypocen-

troidal decomposition algorithm (HDC; Jordan and Sverdrup, 1981). HDC belongs to a class of algorithms used to obtain improved relative earthquake locations through multiple event analysis (e.g., joint hypocentral determination, Dewey, 1972; double difference, Waldhauser and Ellsworth, 2000). Our implementation of HDC is unique among these methods in having been extensively developed for obtaining not only improved relative locations, but also calibrated absolute locations for an entire cluster of events, with reliable estimates of location uncertainty for each event. Examples of the application of the HDC method in calibrated earthquake location studies can be found in Ritzwoller *et al.* (2003), Bondar, Engdahl, *et al.* (2004); Bondar, Myers, *et al.* (2004), Tatar *et al.* (2007), Roustaei *et al.* (2009), and Nissen *et al.* (2010). The key feature of the HDC algorithm is the decomposition. Decomposition greatly facilitates calibrated location studies through orthogonal projection operators, of the multiple-event relocation problem into two independent inverse problems. These independent problems involve (1) the estimation of a set of cluster vectors that describe the location and origin time of each event with respect to a reference location of the hypocentroid that is defined as the geometrical mean of the current locations and origin times and (2) the inversion for an updated location and origin time for the hypocentroid in geographic coordinates, using the relative locations fixed by the cluster vectors and a subset of arrival-time data deemed most suitable for the problem. Separation of the problem in this way permits seismologically appropriate weighting for the two parts of the relocation process, which is critical for obtaining realistic uncertainties of the individual earthquake hypocentral parameters.

Arrival-time data are weighted inversely to the uncertainty of the reading. Unlike most location algorithms, which use *ad hoc* values for data uncertainties for all samples of a given phase, we take advantage of the availability of repeated observations of the same phase at the same station for multiple events in a cluster and use the distribution of residuals from the observed arrival-time data to estimate empirical arrival-time errors for each station-phase pair represented in the data set. These empirical arrival-time errors include traditional reading error and all other sources of variability in the residuals. Empirical arrival-time errors are estimated with a robust statistical method that minimizes the influence of outliers, and we then use the empirical errors to identify and eliminate outliers. This is an iterative process, followed at each step by relocation, repeated until the data set contains only arrival times that are statistically consistent with the observed spread of residuals ($\pm 3\sigma$).

Cluster vectors, which establish the relative location of each event with respect to the hypocentroid, are estimated using all available arrival-time data, regardless of phase type or epicentral distance. This is possible because only travel-time differences are used to estimate improved relative relocations, a common feature in all multiple event relocation algorithms. Therefore, errors in the theoretical travel-time

model used to calculate residuals and derivatives do not propagate significantly into relative location bias.

The key to obtaining calibrated locations for a cluster of events in the HDC method is to locate the hypocentroid of the cluster using only near-source data. This can be done in several ways (e.g., by reference to one or more events in the cluster for which very accurate locations are known independently), but for this study we used arrival-time data at short epicentral distances. In this way, we minimize the biasing effect of the imperfectly known velocity structure in the source region. It is especially important to avoid the use of Moho-refracted phases (Pn , Sn). Because of the dense temporary network, we avoided Moho refracted phases by restricting the data set used for the hypocentroid to distances less than about 60 km and still have a very large number of direct crustal phase arrival times with broad azimuthal coverage.

One disadvantage of the HDC method, in comparison with some other methods of multiple event relocation, is that computational effort grows rapidly with the number of events. To analyze the cluster of 454 events simultaneously would be impractical, so we divided the sequence into three chronological subclusters, each calibrated independently. Preliminary analyses showed that 59 events were not well constrained as part of any subcluster, mainly because of a combination of small numbers of observations and poor azimuthal coverage; these events were dropped. The remaining 395 events for which the locations were calibrated with the HDC analysis are shown in Figure 3 (Table S1, available in the electronic supplement). Each subcluster contains events in all the main regions that were active during this sequence and overlaps in space with the other two subclusters. Therefore, the three clusters can be combined into a single seamless aftershock sequence. Subclusters were compared closely to ensure that there was no significant bias between the three subclusters.

The HDC analysis was also done using the AK135 velocity model (Kennett *et al.*, 1995) in order to maintain consistency with our initial single-event locations. Using a consistent velocity model avoids modest shifts in estimated focal depth (and origin time) between the HDC and initial single-event results. We tested the sensitivity of focal depth to the assumed velocity model by recomputing hypocentroid locations assuming the three-layer velocity model used to locate earthquakes in the CVSZ by the Virginia Tech Seismic Observatory (Chapman, 2013). We found that the hypocentroid (average) depth decreased by 0.2 km (from 5.4 km to 5.2 ± 0.15) and that epicenter locations changed well below the initial uncertainty due to the good azimuthal station coverage for each earthquake. This problem was altogether avoided for the mainshock because depth was constrained by waveform modeling.

Using the travel times relative to the final HDC locations, we then determined an empirical travel-time model for the aftershock sequence. A least-squares fit to travel Pg travel times for distances from 10 to 100 km results in a crustal

P -wave velocity of 6.48 km/s. The empirical fit to Pn travel times at distances from 200 to 1200 km, results in a mantle head wave with a propagation velocity of 8.18 km/s. The intercept time ($T_i = 7.02$ s) determined from the least-squares fit to the mantle head-wave Pn can be used with the crust and mantle velocities to uniquely determine crustal thickness from standard refraction seismology methods (Dobrin and Savit, 1988). Using the velocities determined above, we compute a crustal thickness of 37.3 km. The crustal velocity model derived from our empirical fit to the travel times is very consistent with the lower crust and upper mantle velocity model for the CVSZ discussed in Chapman (2013).

HDC Aftershock Location Results

Figure 3 shows the distribution of 395 relocated aftershocks, both in map view and cross section. Aftershocks are distributed in a nonuniform pattern comprising several small clusters located mostly to the north and east of the mainshock (Fig. 3). Several small shallow clusters are located to the northeast of the largest cluster, toward Lake Anna, and are not associated with known quaternary faults and/or geologic unit boundaries. These clearly defined clusters of shallow seismicity occurred later in the sequence (Table S1, available in the electronic supplement). This suggests that earthquakes in the outer clusters were triggered by stress transfer due to earlier activity in the main cluster.

The main concentration of aftershocks occurs to the west of Mineral, Virginia, along a roughly 8–10 km long northeast-trending cluster, which we infer to be the main portion of the active fault. Profile A–A' on Figure 3, runs perpendicular to the northeast-trending cluster and clearly shows the aftershocks define a southeast-dipping linear feature that we interpret as the active fault (Fig. 3). Aftershocks within this band of seismicity occur primarily in the depth range of about 2.5–8 km. This places the aftershock sequence within the Chopawamsic volcanic belt, which consists of Ordovician age volcanic pluton rocks that accreted to eastern North America during the Taconic Orogeny (Pratt *et al.*, 1988).

We modeled the nearly linear trend of southeast-dipping aftershocks to constrain the orientation of the active fault. We determined the fault dip and strike assuming a simple single plane. The aftershock cluster was chosen to exclude the shallow cluster of events in the northeast of the sequence that appear to represent activity on separate faults (Fig. 3). The shallow cluster is very limited in spatial extent, while deeper events (at 5–8 km depth) have a much stronger influence on the orientation of the planar fit due to their linear extent. A best-fitting fault plane was determined by a least-squares fit to mean depths and locations determined in 0.1 km steps with a width of 0.5 km, through the main aftershock cluster. Figure 4 shows the best-fit single slice through the aftershock cluster. This slice coincides with profile A–A' in Figure 3a, at an azimuth of 126° . The least-squares fit to the mean depth

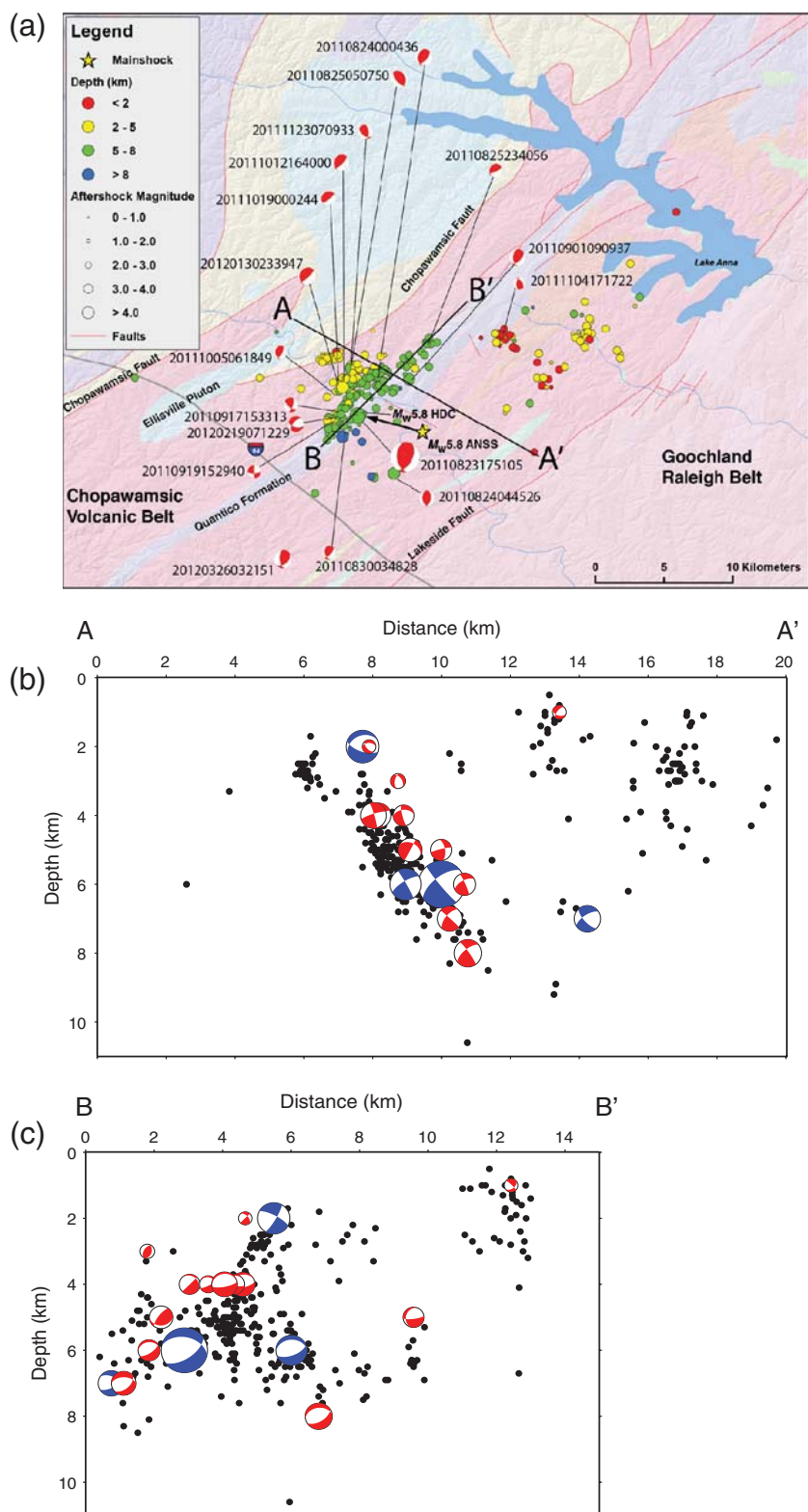


Figure 3. (a) Map and cross sections of the M_w 5.8 Mineral, Virginia, earthquake (August 23 at 17:51:04 UTC) from one year of recording in CVSZ, with the initial ANSS location (yellow star) and the HDC earthquake locations (see also Table S1, available in the electronic supplement). Mapped geologic rock units are from Dicken *et al.* (2008). (b) HDC relocated earthquakes (black circles) and RMT solutions projected onto profile A–A' (38.000° N, –78.045° W to 37.890° N, –77.850° W). (c) HDC relocated earthquakes (black circles) and RMT solutions projected onto profile B–B' (37.900° N, –77.950° W to 38.000° N, –77.900° W). The four RMT solutions determined using only regional waveform data from permanent seismic stations have compressional quadrants shaded in blue in the cross sections, whereas red-shaded solutions include data from the temporary local aftershock network.

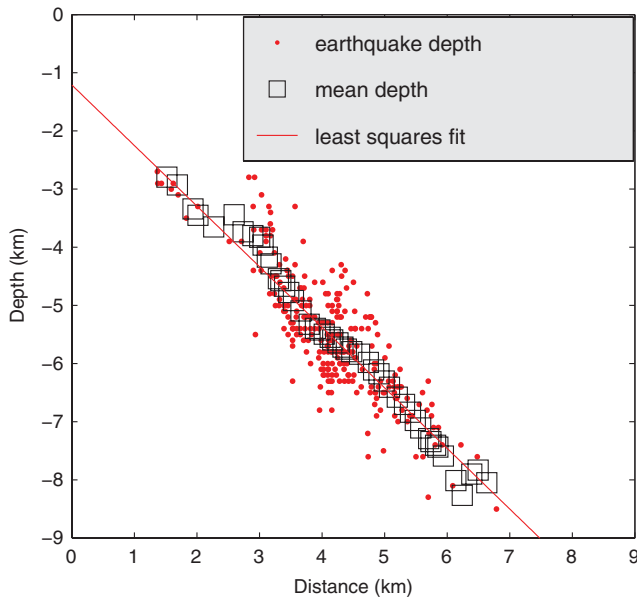


Figure 4. A single slice through the aftershock cluster along the best-fit slice through the aftershock sequence. The slice coincides with profile A–A′ in Figure 3. Endpoints of the slice extend from 38.00° N, −78.05° W to 37.89° N, −77.85° W, with an azimuth of 126°. The least-square fit to the mean depths suggest a 49.5° SE ± 6° dipping fault with a strike of N36°E ± 12°.

indicates a 49.5° southeast-dipping fault with a strike of N36°E. In order to estimate the uncertainty in the fault plane estimate, we applied a bootstrap method where we computed 100 different plane fits with 20% reduction in data. The mean of the 100 different planar fits define a roughly 10 km long fault, that strikes N36°E ± 12° ($\pm 2\sigma$) and dips 49.5° SE ± 6° ($\pm 2\sigma$).

Profile B–B′ in Figure 3 runs roughly parallel to the northeast-trending main cluster and shows a nonuniform depth distribution of aftershocks located along the active fault. A small patch of sparse seismicity to the upper left in the depth range of 2–4 km, and at a distance of 1–3 km along the fault, coincides with a patch of maximum slip and stress drop determined in a finite-fault model for the mainshock (Shao *et al.*, 2011). Based on this observation we suggest that aftershocks in this main cluster occur in regions of the active fault that experienced minimal slip during the mainshock. In the region of maximum slip and stress drop, the majority of crustal strain accumulation was released by the mainshock, and aftershocks occurred on portions of the fault where stress was transferred and increased.

Importantly, the HDC analysis moves the mainshock approximately 5 km to the northwest of the single-event network location provided by the Advanced National Seismic System (ANSS)/Center for Earthquake Research and Information (CERI). The HDC location is within and near the base of the main southeast-dipping aftershock zone. This result is consistent with the relocated mainshock by Chapman (2013). The estimated location error in depth of the mainshock is ± 2 km, whereas the epicentral errors are relatively small

at ± 0.6 km and ± 0.7 km for the semiminor and semimajor axis, respectively (Table S1, available in the electronic supplement to this article). The tight constraint on the mainshock epicentral location is directly due to good absolute locations of aftershocks recorded on both the temporary and permanent stations in the area, which establishes the travel-time corrections needed to properly relocate the mainshock. This demonstrates that the multiple-event HDC method provides improved hypocenters over single-event methods with only regional distance seismic stations available. Station US.CBN was the closest available real-time seismic station to the Mineral, Virginia, mainshock (~ 60 km).

Regional and Teleseismic Moment Tensor Results

Both teleseismic long-period mantle waves (*W*-phase) and regional body wave and surface waves were used to determine the moment magnitude and nodal planes of the mainshock. Green’s functions for the USGS NEIC real-time *W*-phase (Hayes *et al.*, 2009) moment tensor solution were determined using the Preliminary Earth Reference Model global velocity model (Dziewonski and Anderson, 1981), while the regional moment tensor (RMT) method used Green’s functions based on the central United States velocity model of Herrmann, Benz, and Ammon (2011). Given that no aftershocks were well recorded teleseismically, only regional body waves and surface waves were used to determine the moment tensor solutions for several of the larger aftershocks.

The USGS *W*-phase and RMT modeling of the mainshock produced moment estimates of 5.7×10^{17} N·m (M_w 5.77) and 3.8×10^{17} N·m (M_w 5.65), respectively. These differences in moment are within the expected variation based on using different velocity models (Hayes *et al.*, 2013), modeling different frequency bands, and errors associated with the modeling. Nodal planes determined from the both moment tensor methods are relatively insensitive to the velocity model assumption (Hayes *et al.*, 2013).

The mainshock fault solution is modeled as a northeast-trending reverse fault with a strike, dip, and rake for the southeast-dipping nodal plane of 30°, 37°, and 117°, respectively, for the *W* phase and 28°, 50°, and 113°, respectively, for the RMT. These results from both methods are consistent with the best-fit plane to the main cluster of HDC relocated aftershocks discussed above. The *W* phase was modeled in the period band of 50–150 s, thus making it relatively insensitive to precise source depth, particularly in the shallow crust where the event occurred. The *W*-phase moment tensor solution was constrained to a depth of 12 km. The RMT method modeled the waveforms in the period band of 33–100 s, giving it better depth resolution. Using the same procedures as Herrmann, Benz, and Ammon (2011), Figure 5 shows the RMT waveform fit as a function of depth. These results indicate that the RMT method strongly prefers a depth of 6 km, with fit falling off significantly at depths shallower than about 4 km and deeper than about 8 km. The RMT mainshock depth of 6 km is within the uncertainty of the HDC

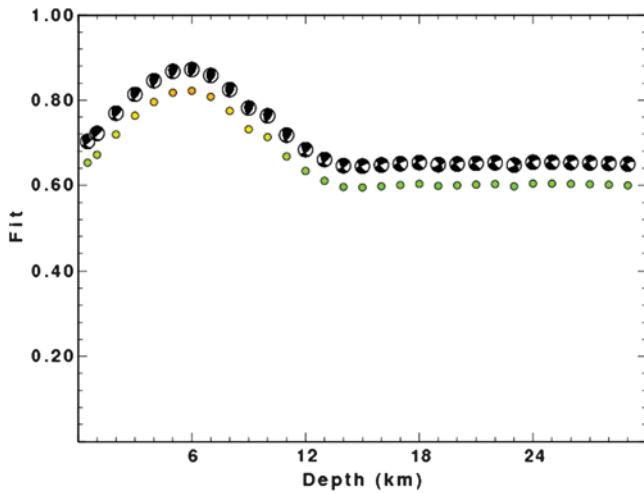


Figure 5. The RMT goodness of fit as a function of source depth for the mainshock. The best-fitting focal mechanism, as determined by the grid search, is shown for each depth. The best fit is at a depth of 6 km.

results (7 ± 2 km). The 1 km difference in depth reflects the different velocity models used. The central United States velocity model of [Herrmann, Benz, and Ammon \(2011\)](#), used for RMT solutions, has a shallow low velocity zone relative to the AK 135 global velocity model used in the HDC analysis.

RMT solutions were computed for 16 aftershocks (Table S2, available in the electronic supplement), which are shown in the cross-sectional view along with all of the relocated aftershocks (Fig. 3). The solutions for the first four events used regional seismic waveforms, whereas data from the local aftershock network were used for the later, smaller events. Successful waveform fit depends upon finding a frequency band in which the signal-to-noise ratio is high and filtered waveforms are still simple. This required individual manual manipulation for the small aftershocks, but we succeeded in modeling some events as small as M_w 1.6. Confidence in the solutions is obtained by focusing on similarity of adjacent mechanisms. Some differences are apparent in the seismicity profiles in Figure 3. The only RMT that varies significantly from the others is the shallow M_w 3.9 aftershock on 25 August 2011 at 05:07 GMT. Is it likely that RMT differences reflect data that were less than optimal because of the large microseisms caused by Hurricane Irene moving along the coast of Virginia at the time of the event. In contrast, the similarity of the shallow M_w 1.6 aftershock on 23 November 2011 at 07:09 that occurred about 1 km away adds confidence to the solution for the M_w 3.9 aftershock (Table S2, available in the electronic supplement), so these shallow events may indicate activity on another fault oblique to the mainshock structure.

Aftershock Magnitude-Frequency Distribution

It is well established that earthquakes are not uniformly distributed in time, space, and magnitude. Distributions of

earthquakes with respect to their magnitudes exhibit (to a first order) scale invariability, appear to be self-similar, and obey a power law or fractal scaling. This implies the absence of a characteristic earthquake (theoretical limits on the maximum event magnitude). An empirical formula

$$\log N = a - bM, \quad (1)$$

known in Japan as the [Ishimoto and Iida \(1939\)](#) relation and in the United States and Europe as the [Gutenberg and Richter \(1942\)](#) relation, defines the distribution of earthquakes with respect to magnitude. For a given region and time interval, equation (1) provides the cumulative number of earthquakes, N , with magnitude, M_w , and larger in which a and b are positive, real constants. a describes the seismic activity (log number of events with $M_w = 0$). The event rate for a certain region depends upon the volume and time window considered; for seismic sequences, this is typically close to $b = 1$. The b -value is a parameter describing the relative abundance of large events with respect to smaller shocks and is related to properties of the seismic medium such as stress and/or material conditions.

Figure 6a shows the cumulative number of earthquakes observed as a function of magnitude, which is used to determine a b -value for the aftershock sequence. For consistency, we only used computed M_L magnitudes because we found them to be accurate over a wide range of magnitudes and distances. Using a maximum likelihood algorithm ([Wiemer, 2001](#)) resulted in a catalog of aftershocks that is complete to M_L 1.1 and has a b -value of 0.75 ± 0.04 (Fig. 6a).

The cumulative number of earthquakes greater than M_L 0.3 as a function of time is plotted in Figure 6b. The plot shows that the seismicity rate changed through time with three distinct phases. The first month of the sequence (September 2011) had the highest rates of seismicity, but then tapered off into the second phase from October 2011 through December 2011. After the beginning of 2012, the rate declined again where it remained relatively constant until the last of aftershock monitoring systems were removed from the field in the summer of 2012.

The distribution of earthquakes as a function of magnitude is plotted in Figure 6c. This histogram is heavily tailed toward the larger magnitudes, with several earthquakes in the magnitude of 3 to 4 range. The histogram distribution demonstrates that the aftershock sequence is dominated by earthquakes ranging from M_L 1.0 to 2.0. This observation is a function of the detection threshold of the network; however, given the b -value observed in Figure 6a, there were likely thousands of undetected aftershocks in the range of M_L 0–1.0. Future studies using waveform cross-correlation methods may help address this issue.

Discussion

This work clearly establishes precise fault geometry and source parameters for an EUS earthquake and its aftershocks

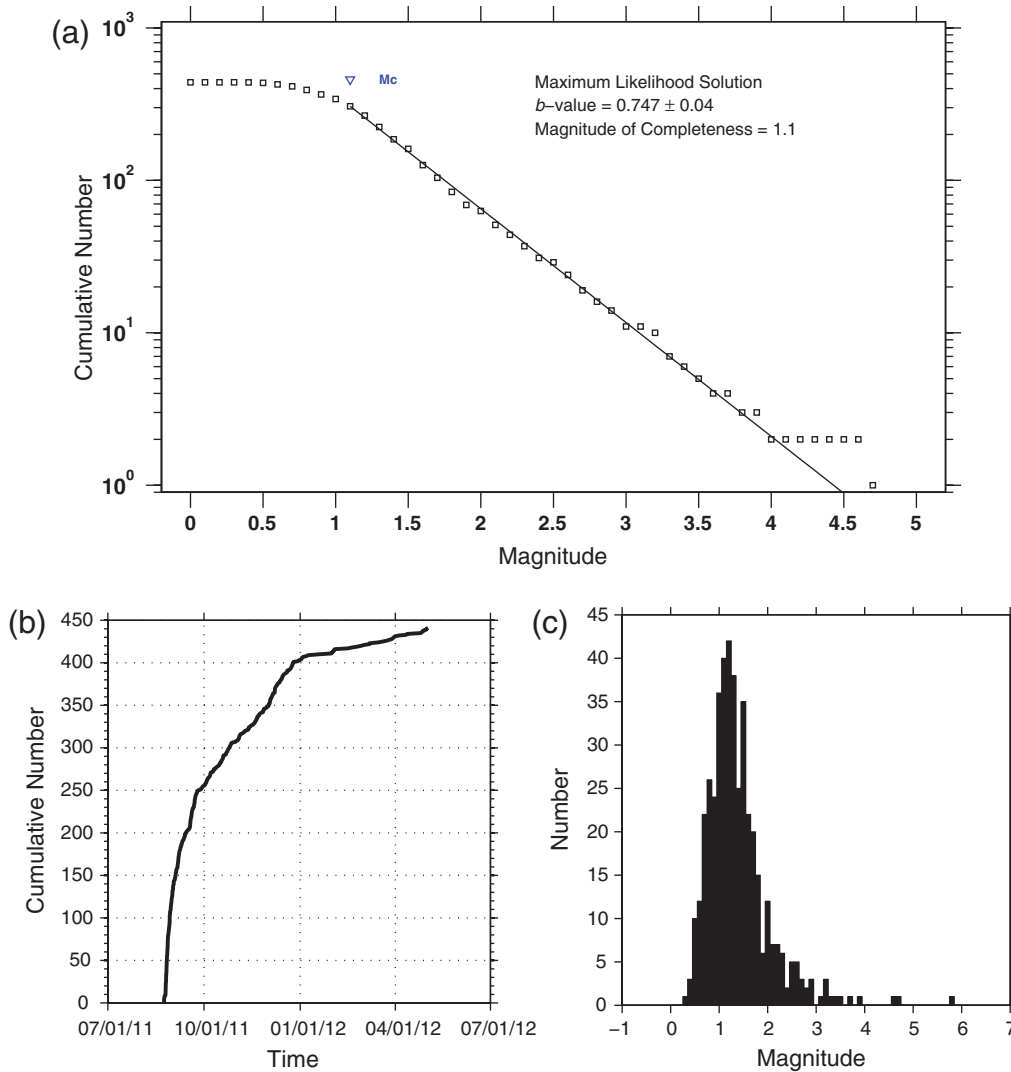


Figure 6. Aftershock statistics of the M_w 5.8 Mineral, Virginia, earthquake using 441 earthquakes from August 2011 to September 2012. For consistency, all magnitudes are M_L . Bounding box defined by the latitude of 37.5° to 38.1° and longitude of -77.0° to -79.0° . (a) Aftershock completeness (M_c) is to a magnitude of M_L 1.1. The distribution has a b -value of 0.75 ± 0.04 . (b) The cumulative number of earthquakes as a function of time shows that seismicity rate changes through time with three distinct phases. (c) Magnitude (M_L) for the M_w 5.8 Mineral, Virginia, aftershock sequence.

based on using modern instrumental data and modeling methods. The spatial distribution of aftershocks reported in this study defines an 8–10 km long fault rupture plane striking $N36^\circ E \pm 12^\circ$ and dipping to the east-southeast at $49.5^\circ \pm 6^\circ$. Fault dimensions, determined by the extent of the aftershocks, are consistent with well-known empirical relations (Wells and Coppersmith, 1994; Leonard, 2010).

Combined aftershock locations and moment tensor solutions indicate that the earthquake was a shallow reverse faulting event that occurred on a southeast-dipping fault with compression in a northwest–southeast direction. This is consistent with the average stress indicators for the EUS that show maximum compression perpendicular to the structural grain of the Appalachian mountains (Zoback, 1992). Waveform modeling of regional phases strongly suggests a shallow mainshock source depth of 6 km, which is consistent

with distribution of near-field macroseismic observations and impact estimated by the USGS ShakeMap and PAGER systems (Wald *et al.*, 1999, 2010, 2011; Hough, 2012). The southeast-dipping trend of aftershocks is within ± 1 s of the predicted dip based on USGS W -phase and RMT modeling of the mainshock. In addition, the estimated strike of the fault plane from W -phase and RMT modeling is within the ± 2 s of the aftershock defined $N36^\circ E \pm 12^\circ$ trend of the active fault plane. The moment tensor results and aftershock seismicity thus show broad consistency, with the mainshock occurring on a northeast-trending, relatively steeply dipping reverse fault.

A crustal scale seismic reflection profile was acquired by the USGS in 1981, approximately 4 km southwest of the nearest aftershocks along highway 64 in central Virginia (Fig. 3). This profile runs nearly perpendicular to the strike of

the aftershock zone and has been interpreted to contain many east-southeast-dipping reverse faults in the allochthonous upper crust of Chopawamsic metavolcanic and Goochland terranes (Harris *et al.*, 1982; Pratt *et al.*, 1988). When projected onto the reflection profile, the aftershocks locate within a relatively nonreflective zone bounded above and below by prominent bands of more shallowly dipping reflectors (T. L. Pratt, *et al.*, unpublished manuscript, 2013). The east-dipping fault, defined by seismicity patterns and moment tensors models, appears to cut through shallowly dipping listric faults that sole out at the decollement at depths of around 6–8 km (Harris *et al.*, 1982; T. L. Pratt, *et al.*, unpublished manuscript, 2013), raising the question of whether or not the earthquake occurred on a new fault or reactivated a pre-existing fault or rock unit contact.

It is useful, from a source scaling perspective, to compare this sequence to that of the 6 April 2009 M_w 6.1 L'Aquila earthquake in Italy (Herrmann, Malagnini, and Munafò, 2011). Aftershocks of both earthquakes were shallow. The L'Aquila earthquake demonstrated normal faulting, whereas the Virginia earthquake exhibited thrusting. The L'Aquila earthquake occurred on an active microplate boundary. Given similar aftershock monitoring capabilities, it is interesting that RMTs could be computed for over 180 L'Aquila aftershocks with $M_w > 3$, whereas only eight of the RMTs determined in this paper had $M_w > 3$. The reason for the differences in the activity of the sequences is not known; however, we suspect stress drop of the mainshock may be a factor. We note the coincidence of a low-productivity CVSZ aftershock sequence following a high stress drop mainshock. Mineral, Virginia, mainshock stress-drop estimates range from 50 to 75 MPa for a circular rupture 1.6–2.0 km in radius based on source corner frequency estimates (Ellsworth *et al.*, 2011) to lower levels based on finite-fault models (average stress drop of 6 MPa and maximum of 16 MPa; Shao *et al.*, 2011) and waveform modeling (30 MPa; Chapman, 2013). In contrast, estimates, using an empirical Green's function method, of L'Aquila earthquake stress drop are lower (10 MPa) than the estimates of the central Virginia earthquake (Poiata *et al.*, 2012; Calderoni *et al.*, 2013).

High stress-drop earthquakes are commonly observed in the EUS, such as for the Saguenay earthquake, in which stress drop was computed at 50 MPa (Boore and Atkinson, 1992) and the 2008 Illinois earthquake, which had a stress drop of 10 MPa (Hartzell and Mendoza, 2011). Stress-drop estimates for the 2011 Mineral, Virginia, mainshock span a wide range but are all higher than the 3–5 MPa commonly found in tectonically active areas such as along the San Andreas fault in California (Imanishi and Ellsworth, 2006). The high stress-drop values for the 2011 Mineral, Virginia, earthquake suggest that there are high levels of stress in mature fault zones of the EUS, which require earthquakes with a nearly complete stress drop for a crust in frictional equilibrium. Because the crust can only support about 100 MPa of differential stress at 5 km depth, the high stress-drop estimate suggests a near-critically stressed crust (Ellsworth *et al.*, 2011).

The cumulative distribution of aftershocks with magnitude is characterized by a low b -value of 0.75 ± 0.04 , suggesting that most of slip or strain release on the fault occurred during the mainshock. This b -value is consistent with a previous broad areal study of earthquake occurrence in the EUS (Okal and Sweet, 2007). This study, along with previous studies of EUS earthquakes, shows that b -values tend to be low, indicating more large events relative to small earthquakes. Our low b -value is consistent with Okal and Sweet (2007), who examined eastern intraplate earthquakes, excluding the New Madrid Seismic Zone, and determined a b -value of 0.69. Aftershock sequences in a wide range of tectonic settings exhibit a range of b -values. For example, a b -value of 0.9 was determined for the 1975 M_w 7.3 Hai-cheng, China, earthquake aftershock sequence (Suyehiro *et al.*, 1964), whereas Wiemer *et al.* (2002) found a higher b -value of 1.2 near the rupture area for the aftershock sequence following the M_w 7.1 Hector Mine, California, earthquake. Wyss (1973) argues that there is an inverse correlation between the observed b -value and the level of stress accumulated in and around the source volume. Regions with low b -value may be interpreted as possible asperities (stress concentrations) reflecting variations in frictional properties along the fault, which may control the recurrence of the next large event.

Infrequent large earthquakes and sparse evidence of neotectonic (~ 2.6 million years ago to the present) earthquake history in the EUS point to the importance of documenting these rare earthquakes to develop scientific insights necessary to improve seismic-hazard assessment in the region. With few earthquakes as large as M_w 5.8 recorded in the EUS, it is difficult to know how typical this behavior is for an aftershock sequence. Considerable scientific uncertainty remains about the nature and scope of the earthquake hazard associated with the CVSZ and similar active source zones in eastern North America. The results presented here provide details of the earthquake source mechanism, location, and its relationship to aftershocks. Studies of this nature are important for improving our estimates of EUS earthquake source scaling and physics and improving national probabilistic seismic-hazards maps.

Data and Resources

Events analyzed include the M_w 5.8 Mineral, Virginia, earthquake of August 2011 and the sequence of aftershocks (Fig. 3; © Table S1, available in the electronic supplement). Data used in this study were digitally recorded at regional broadband stations operated by stations of the USGS, ANSS, and Global Seismic Network (GSN) and 36 portable stations deployed as part of a comprehensive aftershock monitoring project (Fig. 2; Table 1). All waveform data used in this study, from both portable and permanent seismic stations, are archived and available for download from the IRIS Data Management Center (DMC). Analysis and mapping software used includes ZMAP (Wiemer, 2001), SAC (Goldstein *et al.*,

2003; Goldstein and Snoke, 2005), GMT (Wessel and Smith, 1991), and MATLAB. The single-event earthquake location approach used a stand-alone version of USGS NEIC main processing system (HYDRA).

Additional data and resources were obtained from the following websites: USGS global earthquake online database, <http://earthquake.usgs.gov/earthquakes/eqarchives/epic/> (last accessed August 2013); USGS NEIC recent earthquake website, <http://earthquake.usgs.gov/earthquakes/recenteqsww/Quakes/se082311a.php> (last accessed September 2012); the USGS ShakeMap system, <http://earthquake.usgs.gov/earthquakes/dyfi/events/se082311a/us/index.html> (last accessed November 2012); the USGS PAGER system, <http://earthquake.usgs.gov/earthquakes/pager/events/us/082311a/index.html> (last accessed December 2012); the USGS DYFI system, <http://earthquake.usgs.gov/earthquakes/dyfi/events/se082311a/us/index.html> (last accessed November 2012); the USGS *W*-phase system operated by Gavin Hayes, http://earthquake.usgs.gov/earthquakes/eqinthenews/2011/se082311a/se082311a_wmt.php (last accessed January 2013); the USGS Global Centroid Moment Tensor (Global CMT) system, http://earthquake.usgs.gov/earthquakes/eqinthenews/2011/se082311a/se082311a_gcmt.php (last accessed February 2013); the USGS faults and folds database (Machette *et al.*, 2004), <http://earthquake.usgs.gov/hazards/qfaults> (last accessed December 2012); Virginia geologic map data, <http://mrddata.usgs.gov/geology/state/state.php?state=VA> (last accessed February 2013); and the Saint Louis University Earthquake center, <http://www.eas.slu.edu/eqc/eqc20110823.html> (last accessed February 2013).

Details of the RMT source inversion are given at <http://www.eas.slu.edu/eqc/eqc20110823.html> (last accessed March 2013); the EarthScope Transportable array (USArray) (<http://www.usarray.org/researchers/obs/transportable>; last accessed December 2012); the Virginia Tech Seismological Observatory, <http://www.geol.vt.edu/outreach/vtso/> (last accessed January 2013); and CERI, <http://www.ceri.memphis.edu/index.shtml> (last accessed December 2012).

Acknowledgments

This work required a large number of dedicated people. The authors greatly appreciate the rapid response and hard work of the aftershock deployment field crews. The crews included Alena Leeds, Jim Allen, Steve Horton, Won-Young Kim, Noel Barstow, Patrick Bastion, and additional staff from the USGS and Incorporated Research Institutions for Seismology–Program for the Array Seismic Studies of the Continental Lithosphere (IRIS PASSCAL). We would also like to thank staff at the USGS, IRIS PASSCAL, UNAVCO, and station hosts in Louisa County, Virginia, for material and logistical support. Field support for the IRIS PASSCAL stations was provided by National Science Foundation Grant EAR1148357 to Lehigh University. G. Smoczyk provided important detailed maps using ArcMap10.1. Interesting discussions, ideas, and interpretations were provided by A. Shah, T. Pratt, W. Horton, J. Filson, and R. Harrison. J. McCarthy, R. Williams, G. Hayes, and L. Gee provided valuable comments on early versions of the manuscript.

References

- Algermissen, S. T., and D. M. Perkins (1976). A probabilistic estimate of maximum acceleration in rock in the contiguous United States, *U.S. Geol. Surv. Open-File Rept. 76-416*, 45 pp.
- Bollinger, G. A. (1969). Seismicity of the central Appalachian states of Virginia, West Virginia, and Maryland—1758 through 1968, *Bull. Seismol. Soc. Am.* **59**, 2103–2111.
- Bollinger, G. A., and M. G. Hopper (1971). Virginia's two largest earthquakes—December 22, 1875 and May 31, 1897, *Bull. Seismol. Soc. Am.* **61**, no. 4, 1033–1039.
- Bondar, I., E. R. Engdahl, X. P. Yang, H. A. A. Ghalib, A. Hofstetter, V. Kirichenko, R. Wagner, I. Gupta, G. Ekstrom, E. A. Bergman, H. Isrealson, and K. L. McLaughlin (2004). Collection of a reference event set for regional and teleseismic location calibration, *Bull. Seismol. Soc. Am.* **94**, 1528–1545.
- Bondar, I., S. C. Myers, E. R. Engdahl, and E. A. Bergman (2004). Epicentre accuracy based on seismic network criteria, *Geophys. J. Int.* **156**, 483–496.
- Boore, D. M., and G. M. Atkinson (1992). Source spectra for the 1988 Saguenay, Quebec, earthquakes, *Bull. Seismol. Soc. Am.* **82**, 673–719.
- Bradley, D. C. (2008). Passive margins through earth history, *Earth Sci. Rev.* **91**, 1–26.
- Brown, L., D. Quiros, K. Davenport, J. Hole, L. Han, C. Chen, and W. Mooney (2012). Aftershock imaging with dense arrays (AIDA): 3D reflection imaging of local structure using aftershock sources recorded by dense deployment of earthscope portable instruments following the August 23, 2011, M_w 5.8, Virginia earthquake, *Geol. Soc. Am.* **44**, 382.
- Buland, R. P., M. Guy, D. Kragness, J. Patton, B. Erickson, M. Morrison, C. Bryan, D. Ketchum, and H. Benz (2009). Comprehensive seismic monitoring for emergency response and hazards assessment: Recent developments at the USGS National Earthquake Information Center, *American Geophysical Union, Fall Meeting 14–18 December 2009*, Abstract S11B–1696.
- Calderoni, G., A. Rovelli, and S. K. Singh (2013). Stress drop and source scaling of the 2009 April L'Aquila earthquake, *Geophys. J. Int.* **192**, 260–274.
- Campbell, M. R. (1898). Earthquake shocks in Giles County, Virginia, *Science* **7**, 233–235.
- Chapman, M. C. (2005). The seismicity of central Virginia, *Seismol. Res. Lett.* **76**, 115.
- Chapman, M. C. (2013). On the rupture process of the 23 August 2011 Virginia earthquake, *Bull. Seismol. Soc. Am.* **103**, no. 2a, 613–628.
- Dewey, J. (1972). Seismicity and tectonics of western Venezuela, *Bull. Seismol. Soc. Am.* **62**, 1711–1751.
- Dicken, C. L., S. W. Nicholton, J. D. Horton, S. A. Kinney, G. Gunther, M. P. Foose, and J. L. Mueller (2008). Preliminary integrated geologic map databases for the United States: Delaware, Maryland, New York, Pennsylvania, and Virginia, *U.S. Geol. Surv. Open-File Rept. 2005-1325*.
- Dobrin, M. B., and C. H. Savit (1988). Introduction to Geophysical Prospecting, Fourth Ed., McGraw-Hill, Inc., New York, 867 pp.
- Dziewonski, A. M., and D. L. Anderson (1981). Preliminary reference Earth model, *Phys. Earth Planet. In.* **25**, 297–356.
- Earthquake Engineering Research Institute (EERI) (2011). Learning from earthquakes: The M_w 5.8 Virginia earthquake of August 23, 2011, *EERI Special Earthquake Report*, 13 pp., <http://www.eqclearinghouse.org/2011-08-23-virginia/files/2011/12/EERI-GEER-DRC-Virginia-eq-report.pdf> (last accessed September 2013).
- Ellsworth, W. L., K. Imanishi, J. H. Luetgert, J. Kruger, and J. Hamilton (2011). The M_w 5.8 Virginia earthquake of August 23, 2011 and its aftershocks: A shallow high stress drop event, *American Geophysical Union, 2011 Fall Meeting*, San Francisco, California, 14–18 December 2009, Abstract S14B–05.
- Goldstein, P., and A. Snoke (2005). SAC availability for the IRIS community, *DMS Electr. Newsl.* **7**, no. 1, 63 pp.

- Goldstein, P., D. Dodge, M. Firpo, and L. Minner (2003). SAC2000: Signal processing and analysis tools for seismologists and engineers, *Invited Contribution to the IASPEI International Handbook of Earthquake and Engineering Seismology*, W. H. K. Lee, H. Kanamori, P. C. Jennings, and C. Kisslinger (Editors), Academic Press, London.
- Gutenberg, B., and C. F. Richter (1942). Earthquake magnitude, intensity, energy and acceleration, *Bull. Seismol. Soc. Am.* **32**, 163–191.
- Harris, L. D., W. de Witt Jr., and K. C. Bayer (1982). Interpretive seismic profile along interstate 1-64 from the Valley and Ridge to the coastal plain in central Virginia, *U.S. Geol. Surv. Oil and Gas Investigations Chart OC-0123*.
- Hartzell, S., and C. Mendoza (2011). Source, and site response study of the 2008 Mount Carmel, Illinois earthquake, *Bull. Seismol. Soc. Am.* **101**, 951–963.
- Hayes, G. P., E. Bergman, K. Johnson, H. Benz, L. Brown, and A. Melzer (2013). Seismotectonic framework of the February 27, 2010 M_w 8.8 Maule, Chile earthquake sequence, *Geophys. J. Int.* **195**, 1034–1051.
- Hayes, G. P., L. Rivera, and H. Kanamori (2009). Source inversion of the W-Phase: Real-time implementation and extension to low magnitudes, *Seismol. Res. Lett.* **80**, 817–822.
- Herrmann, R. B., H. M. Benz, and C. J. Ammon (2011). Monitoring the earthquake source process in North America, *Bull. Seismol. Soc. Am.* **101**, 2609–2625.
- Herrmann, R. B., L. Malagnini, and I. Munafò (2011). Regional moment tensors of the 2009 L'Aquila earthquake sequence, *Bull. Seismol. Soc. Am.* **101**, 975–993.
- Horton, J. W., and R. A. Williams (2012). The 2011 Virginia earthquake: What are scientists learning? *Eos Trans. AGU* **93**, 33.
- Hough, S. (2012). Initial assessment of the intensity distribution of the 2011 M_w 5.8 Mineral, Virginia earthquake, *Seismol. Res. Lett.* **83**, 649–657.
- Imanishi, K., and W. L. Ellsworth (2006). Source scaling relationships of microearthquakes at Parkfield, CA, determined using the SAFOD pilot hole seismic array, in *Earthquakes: Radiated Energy and the Physics of Faulting*, R. E. Abercrombie, A. McGarr, G. Di Toro, and H. Kanamori (Editors), Geophysical Monograph Series, Vol. 170, American Geophysical Union, Washington, D.C., 81–90.
- Ishimoto, M., and K. Iida (1939). Observations sur les seismes enregistres par le microsismographe construit dernièrement (1), *Bull. Earthquake Res. Inst., Univ. Tokyo* **17**, 443–478.
- Jordan, T. H., and K. A. Sverdrup (1981). Teleseismic location techniques and their application to earthquake clusters in the south-central Pacific, *Bull. Seismol. Soc. Am.* **71**, 1105–1130.
- Kennett, B. L. N., E. R. Engdahl, and R. Buland (1995). Constraints on seismic velocities in the earth from travel times, *Geophys. J. Int.* **122**, 108–124.
- Kim, W., and M. Chapman (2005). The 9 December 2003 Central Virginia earthquake sequence: A compound earthquake in the central Virginia Seismic Zone, *Bull. Seismol. Soc. Am.* **95**, 2428–2445.
- Leonard, M. (2010). Earthquake fault scaling; self-consistent relating of rupture length, width, average displacement, and moment release, *Bull. Seismol. Soc. Am.* **100**, 1971–1988.
- Machette, M., K. Haller, and L. Wald (2004). Quaternary fault and fold database for the nation, *U.S. Geol. Surv. Fact Sheet, 2004-3033*, 2 pp.
- McNamara, M., L. Gee, H. Benz, and M. Chapman (2014). Frequency dependent seismic attenuation in the eastern US as observed from the 2011 central Virginia earthquake and aftershock sequence, *Bull. Seismol. Soc. Am.* **104**, no. 1, doi: [10.1785/0120130045](https://doi.org/10.1785/0120130045).
- Nissen, E., F. Yamini-Fard, M. Tatar, A. Gholamzadeh, E. A. Bergman, J. R. Elliot, J. A. Jackson, and B. E. Parsons (2010). The vertical separation of mainshock rupture and microseismicity at Qeshm island in the Zagros fold-and-thrust belt, Iran, *Earth Planet. Sci. Lett.* **296**, 181–194.
- Okal, E. A., and J. R. Sweet (2007). Frequency-size distributions for intraplate earthquakes, in *Continental Intraplate Earthquakes: Science, Hazard, and Policy Issues*, S. Stein and S. Mazzotti (Editors), Geological Society of America Special Paper 425, 59–71.
- Petersen, M. D., A. D. Frankel, S. C. Harmsen, C. S. Mueller, K. M. Haller, R. L. Wheeler, R. L. Wesson, Y. Zeng, O. S. Boyd, D. M. Perkins, N. Luco, E. H. Field, C. J. Wills, and K. S. Rukstales (2008). Documentation for the 2008 Update of the United States National Seismic Hazard Maps, *U.S. Geol. Surv. Open-File Rept. 2008-1128*, 61 pp.
- Poiata, N., K. Koketsu, A. Vuan, and H. Miyake (2012). Low-frequency and broad-band source models for the 2009 L'Aquila, Italy, earthquake, *Geophys. J. Int.* **191**, 224–242.
- Pratt, T. L., C. Coruh, and J. K. Costain (1988). A geophysical study of the Earth's crust in central Virginia: Implications for Appalachian crustal structure, *J. Geophys. Res.* **93**, 6649–6667.
- Ritzwoller, M. H., N. M. Shapiro, A. L. Levshin, E. A. Bergman, and E. R. Engdahl (2003). The ability of a global 3-D model to locate regional events, *J. Geophys. Res.* **108**, 2353–2377.
- Roustaei, M., E. Nissen, M. R. Abbassi, M. Ghorashi, A. Gholamzadeh, M. Tatar, F. Yamini-Fard, E. A. Bergman, J. A. Jackson, and B. E. Parsons (2009). Vertical separation of surface folding, earthquake faulting, and aftershocks in the Zagros Simply Folded Belt (Iran), *Geophys. J. Int.* **142**, 1–24.
- Shao, G., J. Crempien, R. J. Archeleta, and C. Ji (2011). Rupture process and stress drop of the 2011 M_w 5.8 Virginia earthquake based on seismic waveforms, *American Geophysical Union, Fall Meeting 2011*, San Francisco, California, 5–9 December 2011, Abstract S11B–2237.
- Stein, S., S. Cloetingh, N. Sleep, and R. Wortel (1989). Passive margin earthquakes, stresses, and rheology, in *Earthquakes at North-Atlantic Passive Margins*, S. Gregerson and P. Basham (Editors), Kluwer, Dordrecht, The Netherlands, 231–260.
- Suyehiro, S., T. Asada, and M. Ohtake (1964). Foreshocks and aftershocks accompanying a perceptible earthquake in central Japan, *Pap. Meteorol. Geophys.* **15**, 71–88.
- Tatar, M., J. A. Jackson, D. Hatzfeld, and E. A. Bergman (2007). The 2004 May 2, Baladeh earthquake (M_w 6.2) in the Alborz, Iran: Overthrusting the South Caspian Basin margin, partitioning of oblique convergence and the seismic hazards of Tehran, *Geophys. J. Int.* **170**, 249–261.
- Wald, D. J., K. S. Jaiswal, K. D. Marano, D. B. Bausch, and M. G. Hearne (2010). PAGER—Rapid assessment of an earthquake's impact, *U.S. Geol. Surv. Fact Sheet 2010-3036*, 4 pp.
- Wald, D. J., V. Quitoriano, T. H. Heaton, H. Kanamori, C. W. Scrivner, and B. C. Worden (1999). TriNet “ShakeMaps”—Rapid generation of peak ground-motion and intensity maps for earthquakes in southern California, *Earthq. Spectra* **15**, no. 3, 537–556.
- Wald, D. J., V. Quitoriano, C. B. Worden, M. Hopper, and J. W. Dewey (2011). USGS “Did You Feel It?” Internet-based macroseismic intensity maps, *Ann. Geophys.* **54**, 6.
- Waldhauser, F., and W. L. Ellsworth (2000). A double-difference earthquake location algorithm: Method and application to the northern Hayward fault, California, *Bull. Seismol. Soc. Am.* **90**, no. 6, 1353–1368.
- Wells, D. L., and K. J. Coppersmith (1994). New empirical relationships among magnitude, rupture length, rupture width, rupture area, and surface displacement, *Bull. Seismol. Soc. Am.* **84**, 974–1002.
- Wessel, P., and W. Smith (1991). Free software helps display data, *Eos Trans. AGU* **72**, 445–446.
- Wiemer, S. (2001). A software package to analyze seismicity: ZMAP, *Seismol. Res. Lett.* **72**, 373–382.
- Wiemer, S., M. Gerstenberger, and E. Hauksson (2002). Properties of the Aftershock Sequence of the Hector Mine Earthquake: Implications for Aftershock Hazard, *Bull. Seismol. Soc. Am.* **92**, 1227–1240.
- Wilson, J. T. (1965). A new class of faults and their bearing on continental drift, *Nature* **207**, 343–347, doi: [10.1038/207343a0](https://doi.org/10.1038/207343a0).
- Wolin, E., S. Stein, F. Pazzaglia, A. Meltzer, A. Kafka, and C. Berti (2012). Mineral, Virginia, earthquake illustrates seismicity of a passive-aggressive margin, *Geophys. Res. Lett.* **39**, doi: [10.1029/2011GL050310](https://doi.org/10.1029/2011GL050310).
- Wyss, M. (1973). Towards a physical understanding of the earthquake frequency distribution, *Geophys. J. Roy. Astron. Soc.* **31**, 341–359.

Zoback, M. L. (1992). Stress field constraints on intraplate seismicity in eastern North America, *J. Geophys. Res.* **97**, 11,761–11,782, doi: [10.1029/92JB00221](https://doi.org/10.1029/92JB00221).

U.S. Geological Survey
MS966, Box 25046
Denver, Colorado 80225
(D.E.M., H.M.B., P.E.)

Department of Earth and Atmospheric Sciences
3642 Lindell Boulevard
Saint Louis University
St. Louis, Missouri 63108
(R.B.H.)

Global Seismological Services
1900 19th Street
Golden, Colorado 80401
(E.A.B.)

Department of Earth and Environmental Sciences
1 West Packer Avenue
Lehigh University
Bethlehem, Pennsylvania 18015
(A.M.)

Center for Earthquake Research and Information (CERI)
University of Memphis
3890 Central Ave.
Memphis, Tennessee 38152
(M.W.)

Department of Geosciences
4044 Derring Hall, Virginia Tech
Blacksburg, Virginia 24061
(M.C.)

Manuscript received 5 March 2013;
Published Online 24 December 2013